Wrench and Twist Capability Analysis for Cable-Driven Parallel Robots With Consideration of the Actuator Torque–Speed Relationship

Arthur Ngo Foon Chan, *Member, IEEE*, Sabrina Wai Yi Lam, and Darwin Lau, *Senior Member, IEEE*

***Abstract*—The wrench feasibility and twist feasibility are the workspace conditions that indicate whether the mobile-platform (MP) of the cable-driven parallel robots (CDPRs) can provide a sufficient amount of wrench and twist. Traditionally, these two quantities are evaluated independently from the actuator's torque and speed limits, which are assumed to be fixed in the literature, but they are, indeed, coupled. This results in a conservative usage of the actuator capability and, hence, hinders the robot's actual feasibility. In this study, new approaches to analyzing and commanding CDPRs by considering the coupling effect are proposed. First, the required wrench of the MP is mapped into the twist space by the motors' torque–speed relationship and becomes the wrench-dependent available twist set. Then, a new workspace condition and a new metric are introduced based on the available twist set. The metric shows the maximum allowable MP speed map of the workspace. Finally, a varying speed trajectory is designed based on the metric to optimize the total MP traveling time. This study shows the potential of robot wrench–twist capability and enhances the robot hardware effectiveness without any hardware changes.**

***Index Terms*—Manipulation planning, parallel robots, tendon/wire mechanism, wrench-twist feasibility.**

I. Introduction

CABLE-DRIVEN parallel robots (CDPRs) are a type of parallel mechanism in which the motion and wrench of the moving platform (MP) are produced by a set of actuated cables within a rigid frame. The primary advantages of CDPRs include their higher payload-to-weight ratio [1], larger potential workspace [2], higher reconfigurability, and higher transportability. As a result, numerous unique applications using CDPRs have been proposed, including heavy material handling within warehouses [3], large-scale laser cutting and engraving [4], building construction [5], and stadium sports cameras [6]. The primary unique characteristic of CDPRs is that the cables can only pull but not push (*positive cable forces*).

As a result, CDPRs require actuation redundancy in order to fully constrain the system [7]. This creates challenges in analyzing its workspace [8], [9], [10], [11], [12], inverse dynamics [13], [14], and control [15]. In addition to the positive cable force constraint, lower and upper bounds on cable forces must also be considered in the analysis of CDPRs. In real-world applications, the lower force bounds prevent the cables from becoming slack [16] and the upper force bounds result from the maximum torque that the actuators can provide. These bounds limit the MP wrench that could be delivered. Similarly, there exist maximum bounds on the cable speed that limit the range of MP twists that can be produced [17]. The actuation redundancy, force, and speed bounds together complicate the analysis of CDPRs.

Workspace analysis is a typical tool used to understand the capabilities of the MP given specific requirements. Relating to the CDPR dynamics, typical types of workspace include the static [8], [18], wrench closure [19], [20], and wrench feasible [11] workspaces. Among these, the wrench feasible workspace (WFW) is the most general, defined as the poses where a *required wrench set* (RWS) belongs within the *available wrench set* (AWS) produced by the projection of the bounded cable forces onto the MP wrench space. Relating to the CDPR kinematics, the twist feasible workspace (TFW) [21], [22] is similar to WFW but uses the cable speed bounds to compute the *available twist set* (ATS), that is, the set of possible MP velocities. The WFW and TFW analyses are vital to study the wrenches and twists that can be produced, to plan the robot motion, and to design the CDPR cable attachments. Recently, the working region of the CDPR has been increased based on the workspace analysis, which was achieved by either using a passive counterbalancing mechanism [23] or an optimized unmanned aerial vehicle arrangement for the aerial cable towed robot [24]. By considering the wrench sets, an effective actuator set is presented in [25]. It is done by finding the lowest upper cable force bound such that a generated AWS could best fit the RWS.

In existing wrench and twist analysis studies, one major simplifying assumption is that the maximum cable forces and speeds are constant and independent of each other. This simplifies the analysis and understanding of the wrench and

Manuscript received 23 November 2022; revised 12 March 2023; accepted 1 April 2023. Date of publication 1 May 2023; date of current version 8 August 2023. The work was supported in part by the Research Grants Council (General Research Fund Reference No. 14206419 and Theme-Based Research Scheme Reference No. T42-409/18-R) and in part by the Innovation and Technology Commission (University-Industry Collaboration Programme Reference No. UIM/345). This paper was recommended for publication by Associate Editor Marc Gouttefarde.

The authors are with the Department of Mechanical and Automation Engineering, The Chinese University of Hong Kong, Hong Kong SAR, China (e-mail: foonchan44@link.cuhk.edu.hk; lwy0100@gmail.com; darwinlau@cuhk.edu.hk).

This article has supplementary material provided by the authors and color versions of one or more figures available at https://doi.org/10.1109/TRO.2023.3267383.

Digital Object Identifier 10.1109/TRO.2023.3267383

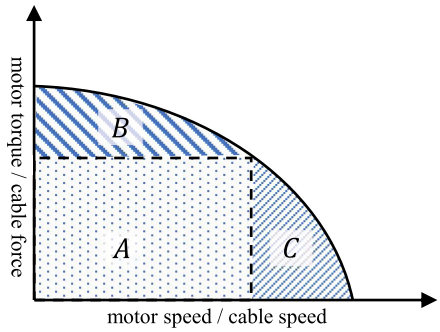

Fig. 1. Typical motor force–speed curve.

twist execution of CDPRs in two ways. First, any combination of cable forces and speeds within the maximum bounds can be arbitrarily selected to be used to command the robot. Second, the AWS and ATS can be independently generated during the capability analysis, and all twists and wrenches within the AWS and ATS can be fully executed. However, the constant maximum cable force and speed assumption do not reflect the true varying maximum torque–speed relationship that is caused by the back-electromotive force (EMF) [26].

For direct-current motors, the increase in their rotational speed also increases the back EMF and, hence, decreases the maximum possible motor current/torque. As such, a motor can provide higher maximum torques when it operates at lower speeds and vice versa. The *force–speed curve*,[1] as shown in Fig. 1, represents the relationship between the maximum deliverable torque and rotational speed of the actuator. Thus, the area under the curve represents the complete set of operating conditions for the motor. Under the assumption of constant maximum cable force and speed, the actuator's operating conditions would be a rectangular region, such as region A of Fig. 1.

As can be observed, the rectangular force–speed region underestimates the full operational capabilities of the actuators and does not consider the following cases. First, for wrenches that are outside the AWS under a fixed maximum cable force and speed bounds, it may be possible that it can still be executed but with a reduced robot speed (region B of Fig. 1). Second, for wrenches that do not require the maximum cable force to execute, it may be possible to operate the robot at a higher speed beyond that of the constant maximum cable speed (region C of Fig. 1). Both of these cases show that the capabilities of the actuators are conservatively used under the assumption of maximum cable forces and speeds. Moreover, another important challenge that arises under the assumption is the suitable selection of the maximum cable force and speed operating point from the actuator's force–speed curve.

As observed from the motor curve, the choice of fixed maximum cable force and speed is an inevitable compromise. This is particularly important as the maximum cable force and speed are assumed to be the same for all poses. If a higher maximum cable force is selected, due to the requirement of particular poses, then the robot would suffer from a lower maximum operational speed for all poses. On the contrary, to achieve a higher maximum speed, then the CDPR would have a decreased wrench-producing capability. To resolve these issues, CDPR analyses should consider the actuator's force–speed curve. However, this couples the feasible cable forces and speeds and, hence, the AWS and ATS. As a result, this complicates the study of CDPR WFW and TFW analysis and mobile-platform (MP) motion generation.

In this article, novel methods are proposed for the analysis of the wrench and twist sets for CDPR that incorporate the actuator's force–speed profile. First, it is shown that a required wrench-dependent ATS (RWDATS) can be generated from a desired wrench set requirement for a force–speed profile, defined as a piecewise set of linear and quadratic relationships. It is shown that the boundary equations of the RWDATS can be expressed by a set of paraboloids. The maximum speed to travel in any direction at a given pose can be conveniently determined from the RWDATS. Subsequently, the RWDATS is used to derive a new type of combined wrench–twist feasible workspace (WTFW) that considers the full capability of the actuators. Furthermore, it is shown that for the desired traveling direction of the MP, the maximum speed in that particular direction can be computed by solving a quadratically constrained program (QCP). This can be used to produce a time-optimal trajectory for a given motion path. The proposed method is compared with the typical rectangular force–speed profile by a 6-degree-of-freedom (DoF) CDPR.

The rest of this article is organized as follows: Section II presents the background to the modeling and wrench analysis of CDPRs. Section III proposes the available wrench–twist sets. This is used to compute the WTFW in Section IV. Section V derives the maximum speed for a path to achieve time and optimal trajectory. Sections VI and VII show the results of the proposed methods in the simulation and on the hardware, respectively. Finally, Section VIII concludes this article.

II. CDPR Wrench Sets and Twist Sets

In this section, the kinematics and dynamics models for all n-DoF CDPR actuated by m-cables, as shown in Fig. 2, are presented. The MP pose is defined by its position and orientation represented by the vector $\boldsymbol{p}(\boldsymbol{q}) \in \mathbb{R}^3$ and rotation matrix ${}^0_E\boldsymbol{R}(\boldsymbol{q}) \in \mathbb{R}^{3\times3}$, respectively. The vector $\boldsymbol{q} \in \mathbb{R}^n$ represents the generalized coordinates of the CDPR. The rotation matrix represents the rotation between the base frame $\{0\}$ and the MP frame $\{E\}$. The vectors ${}^0\boldsymbol{a}_i$ and ${}^E\boldsymbol{b}_i$ represent the positions of the base with respect to the frame $\{0\}$ and MP cable attachments of cable i with respect to the frame $\{E\}$, respectively. The cable vector $\boldsymbol{l}_i \in \mathbb{R}^3$ for cable i can be expressed as

$$\boldsymbol{l}_i = {}^0\boldsymbol{p}(\boldsymbol{q}) - {}^0\boldsymbol{a}_i + {}^0_E\boldsymbol{R}(\boldsymbol{q}){}^E\boldsymbol{b}_i. \tag{1}$$

The length $l_i \in \mathbb{R}$ of cable i is, hence, the two-norm of the cable vector, where $l_i = \|\boldsymbol{l}_i\|_2 = \boldsymbol{l}_i^T\boldsymbol{l}_i$. Let $\boldsymbol{l} \in \mathbb{R}^m$ be the cable length vector storing all of the cable lengths

$$\boldsymbol{l} = [l_1,\ l_2, \ldots,\ l_m]^T. \tag{2}$$

[1]It is assumed that the cables are actuated with fixed diameter spools, and hence, the relationships between cable force and motor torque, and cable speed and motor speed are linear.

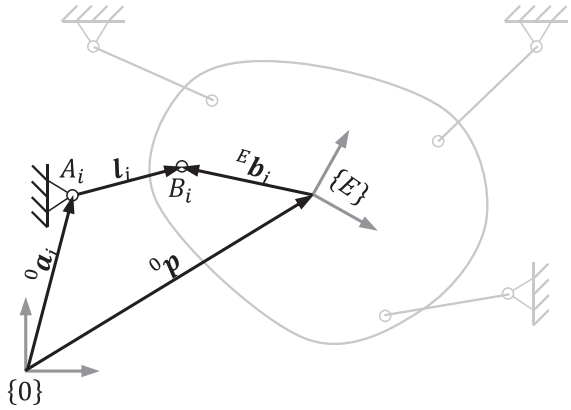

Fig. 2. Model of a 3-DoF planar CDPR.

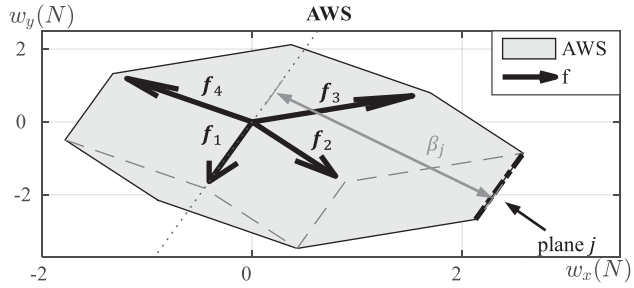

Fig. 3. AWS example for a 2-DoF, 4 cables CDPR. In this particular MP pose, the set boundary is formed by eight hyperplanes. Plane j is highlighted and it is a projection of cable force $\boldsymbol{f}_1$. It is projected by $\boldsymbol{f}_2$ and $\boldsymbol{f}_3$ (i.e., $\mathcal{Z}_j = 2, 3$). β_j is the perpendicular distance from the origin to the jth plane.

Differentiating (2) with respect to time gives the relationship between cable and MP twist, that is

$$\dot{\boldsymbol{l}} = \boldsymbol{J}(\boldsymbol{q})\dot{\boldsymbol{q}}. \tag{3}$$

It represents the inverse kinematic of the CDPR and $\boldsymbol{J} \in \mathbb{R}^{m\times n}$ is the Jacobian matrix. For the system dynamics, the effective wrench $\boldsymbol{w} \in \mathbb{R}^n$ applied on the MP is directly related to the cable force $\boldsymbol{f}$ [15], by the relationship

$$\boldsymbol{w} = \boldsymbol{M}(\boldsymbol{q})\ddot{\boldsymbol{q}} + \boldsymbol{C}(\boldsymbol{q}, \dot{\boldsymbol{q}}) + \boldsymbol{g}(\boldsymbol{q}) + \boldsymbol{w}_{\text{ext}} = -\boldsymbol{J}^T(\boldsymbol{q})\boldsymbol{f} \tag{4}$$

where $\boldsymbol{M} \in \mathbb{R}^{n\times n}$, $\boldsymbol{C} \in \mathbb{R}^n$, $\boldsymbol{g} \in \mathbb{R}^n$, and $\boldsymbol{w}_{\text{ext}} \in \mathbb{R}^n$ are the mass–inertia matrix, centrifugal and Coriolis vector, gravity vector, and external disturbance acting to the MP, respectively. Similar to the cable vector, the cable force vector $\boldsymbol{f} = [f_1,\ f_2, \ldots,\ f_m]^T$ encapsulates the force for every cable.

A. Wrench Sets

Wrench sets $\mathcal{W} \subseteq \mathbb{R}^n$ represent collections of wrenches, $\boldsymbol{w} \in \mathcal{W}$. Two types of wrench sets that are significant to the CDPR analysis are the RWS and the AWS. The RWS, $\mathcal{W}_{\text{r}}$ is a user-defined set that contains desired MP wrenches. It includes the mass–inertia acceleration, centrifugal and Coriolis wrench, gravitational force, and external wrench that were shown in (4). If the components are uncertain during the robot operation, they could be approximated by setting an upper bound and could be included in the set.

On the other hand, the AWS, $\mathcal{W}_{\text{a}}$ describes the set of possible wrenches that the MP can produce based on the constraint on the cable forces. Mathematically

$$\mathcal{W}_{\text{a}}(\boldsymbol{q}) = \{\boldsymbol{w} \in \mathbb{R}^n : \boldsymbol{w} = \boldsymbol{J}^T(\boldsymbol{q})\boldsymbol{f},\ \underline{\boldsymbol{f}} \preceq \boldsymbol{f} \preceq \overline{\boldsymbol{f}}\} \tag{5}$$

where $\underline{\boldsymbol{f}}$ and $\overline{\boldsymbol{f}}$ are the vectors of the minimum and maximum cable force bounds, respectively. Geometrically, the AWS under fixed cable force bounds in (5) is a zonotope [27], [28], [29]. As such, an AWS with p-number of hyperplane boundaries could be alternatively represented by a set of p linear inequalities and mathematically defined as

$$\mathcal{W}_{\text{a}}(\boldsymbol{q}) = \{\boldsymbol{w} \in \mathbb{R}^n : \boldsymbol{\alpha}_j^T(\boldsymbol{q})\boldsymbol{w} \le \beta_j(\boldsymbol{q}, \overline{\boldsymbol{f}})\} \tag{6}$$

where $\boldsymbol{\alpha}_j \in \mathbb{R}^n$ and $\beta_j \in \mathbb{R}$ define the zonotope jth half-space with $j = 1, \ldots, p$. Each of them is contributed by combinations of cable forces. Let p numbers of integer sets be $\mathcal{Z}_j$, $j = 1, \ldots, p$. Each $\mathcal{Z}_j$ contains all indices of cable forces that are contributing to the jth half-space. Fig. 3 explains the concept.

Using the RWS and AWS, the *wrench feasible condition* (WFC) [30] at a pose $\boldsymbol{q}$ is satisfied if the RWS is a subset of the AWS, i.e., $\mathcal{W}_{\text{r}} \subseteq \mathcal{W}_{\text{a}}(\boldsymbol{q})$. Assuming that the RWS is also a convex set, then the WFC can be evaluated just by checking whether all vertices of the RWS are included in the AWS. Suppose that there are q numbers of extreme points in $\mathcal{W}_{\text{r}}$, namely $\boldsymbol{w}_1^{\text{r}}, \ldots, \boldsymbol{w}_q^{\text{r}} \in \mathcal{W}_{\text{r}}$. A pose is said to be wrench feasible if and only if

$$\boldsymbol{\alpha}_j^T(\boldsymbol{q})\boldsymbol{w}_k^{\text{r}} \le \beta_j(\boldsymbol{q}, \overline{\boldsymbol{f}}) \quad \forall j = 1, \ldots, p \quad \forall k = 1, \ldots, q. \tag{7}$$

Using the WFC, the WFW refers to the set of poses that satisfies the WFC

$$\text{WFW} = \{\boldsymbol{q} : \boldsymbol{w} = -\boldsymbol{J}^T(\boldsymbol{q})\boldsymbol{f} \quad \forall \boldsymbol{w} \in \mathcal{W}_{\text{r}},\ \exists \boldsymbol{f} \in [\underline{\boldsymbol{f}}, \overline{\boldsymbol{f}}]\}. \tag{8}$$

B. Twist Sets

Twist sets $\mathcal{T} \subseteq \mathbb{R}^n$ represent different sets of twists (velocities), $\dot{\boldsymbol{q}} \in \mathbb{R}^n$ from (3). The ATS, $\mathcal{T}_{\text{a}}$ refers to the set of twists that can be generated for a given range of cable length velocities. The set could be written as

$$\mathcal{T}_{\text{a}}(\boldsymbol{q}) = \{\dot{\boldsymbol{q}} \in \mathbb{R}^n : \boldsymbol{J}\dot{\boldsymbol{q}} = \dot{\boldsymbol{l}},\ \underline{\dot{\boldsymbol{l}}} \preceq \dot{\boldsymbol{l}} \preceq \overline{\dot{\boldsymbol{l}}}\} \tag{9}$$

where $\underline{\dot{\boldsymbol{l}}}$ and $\overline{\dot{\boldsymbol{l}}}$ are the vectors of the minimum and maximum cable velocity bounds, respectively, and $\boldsymbol{J}^\dagger$ is the pseudoinverse of $\boldsymbol{J}$. Geometrically, the ATS under fixed cable force bounds in (9) is also a zonotope [17]. It is written as

$$\mathcal{T}_{\text{a}}(\boldsymbol{q}) = \{\dot{\boldsymbol{q}} \in \mathbb{R}^n : \boldsymbol{\gamma}_j^T(\boldsymbol{q})\dot{\boldsymbol{q}} \le \delta_j(\boldsymbol{q}, \underline{\dot{\boldsymbol{l}}}, \overline{\dot{\boldsymbol{l}}})\} \tag{10}$$

where $\boldsymbol{\gamma}_j \in \mathbb{R}^n$ and $\delta_j \in \mathbb{R}$ define the zonotope jth half-space with $j = 1, \ldots, p$. Similar to (7), if the required twist set (RTS) is a convex set with q number of extreme points, i.e., $\dot{\boldsymbol{q}}_1^{\text{r}}, \ldots, \dot{\boldsymbol{q}}_q^{\text{r}} \in \mathcal{T}_{\text{r}}$ A pose is said to twist feasible if and only if

$$\boldsymbol{\gamma}_j^T(\boldsymbol{q})\dot{\boldsymbol{q}}_k^{\text{r}} \le \delta_j(\boldsymbol{q}, \underline{\dot{\boldsymbol{l}}}, \overline{\dot{\boldsymbol{l}}}) \quad \forall j = 1, \ldots, p \quad \forall k = 1, \ldots, q. \tag{11}$$

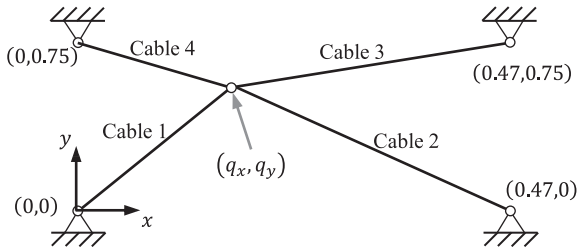

Fig. 4. 2-DoF planar CDPR example.

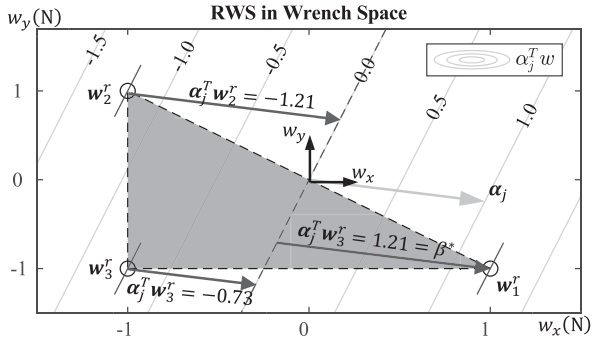

Fig. 5. Perpendicular distance to different vertices of $\mathcal{W}_\mathrm{r}$. For plane j, the maximum perpendicular distance β_j^* is 1.21.

III. ATS Generation From the Required Wrenches

To evaluate the MP feasibility of wrench and twist simultaneously, it is required to check whether both the RWS and the RTS are inside the AWS and ATS, respectively. Under the constant maximum motor torque and speed assumption, the available sets are independent, and hence, the feasibility could be evaluated individually by (6) and (10).

However, this approach cannot be applied when the full motor capability of the torque–speed profile is considered. To solve this problem, the concept of a wrench–twist pair (W–T pair) is proposed. The W–T pair is comprised of two sets, which are defined in wrench and twist space. The user has to design the RWS first; then, the dependent ATS would be calculated. This dependent ATS captures the coupling effect from the motor torque–speed relationship and, hence, fully reveals the robot's capability under the user's requirement.

In this section, the dc motor curve will first be modeled. It will also illustrate how the choice of fixed motor operation points affects the shape of the AWS and the ATS. Next, it will show how the set RWDATS is calculated. A 4-cable point mass 2-DoF planar CDPR (refer to Fig. 4) would be used as an example in the following sections. The attachment points on the frame are $[0,0]^T, [0.47,0]^T, [0.47,0.75]^T, [0,0.75]^T$. The RWS is a triangle with vertices $\mathcal{W}_\mathrm{r} = \{(-1,-1),(-1,1),(1,-1)\}$ (ref to Fig. 5).

A. Cable Force–Speed Model

The maximum deliverable torque of a dc motor is inversely related to its operating speed, similar to that shown in Fig. 1. It is due to the increase of the back EMF when the motor rotates at a higher speed. The back EMF hinders the current that passes through the motor coil; hence, the deliverable torque decreases when the motor speed increase. The torque–speed curve boundary of the ith motor can be modeled as s number of piecewise concave downward quadratic functions

$$\overline{\tau}_i(\dot{\theta}) = \begin{cases} \overline{\tau}_{i,1}(\dot{\theta}), & \dot{\theta}_{i,0} \le \dot{\theta} < \dot{\theta}_{i,1} \\ \quad\vdots & \\ \overline{\tau}_{i,s}(\dot{\theta}), & \dot{\theta}_{i,s-1} \le \dot{\theta} < \dot{\theta}_{i.s} \end{cases} \tag{12}$$

where

$$\overline{\tau}_{i,l}(\dot{\theta}) = c_{i,l}\dot{\theta}^2 + b_{i,l}\dot{\theta} + a_{i,l} \tag{13}$$

and τ is the motor torque, $\dot{\theta}$ is the angular velocity of the motor, and $(c_{i,l}, b_{i,l}, a_{i,l})$ are the coefficients of torque–speed curve at l segment. The quadratic function for each segment could be obtained by quantile quadratic regression. Although (12) could be constructed by any finite number of quadratic functions, two quadratic functions and two linear functions usually are sufficient to represent most of the motor curves of dc motors.

Assuming that all cables of the CDPRs are actuated by fixed radius spools with radius R, the relationship between the cable force f and motor torque is $\tau = R \cdot f$, and the relationship between cable speed and motor speed can be expressed as $\dot{l} = R \cdot \dot{\theta}$. Hence, from (13), the ith cable force–speed relationship can be expressed as

$$\overline{f}_i(\dot{l}) = \begin{cases} \overline{f}_{i,1}(\dot{l}), & R_i \cdot \dot{\theta}_{i,0} \le \dot{l}_i \le R_i \cdot \dot{\theta}_{i,1} \\ \quad\vdots & \\ \overline{f}_{i,s}(\dot{l}), & R_i \cdot \dot{\theta}_{i,s-1} \le \dot{l}_i \le R_i \cdot \dot{\theta}_{i,s} \end{cases} \tag{14}$$

where

$$\begin{aligned} \overline{f}_{i,l}(\dot{l}_i) &= \frac{c_{i,l}}{R_i^3}\dot{l}_i^2 + \frac{b_{i,l}}{R_i^2}\dot{l}_i + \frac{a_{i,l}}{R} \\ &:= \overline{c}_{i,l}\dot{l}_i^2 + \overline{b}_{i,l}\dot{l}_i + \overline{a}_{i,l}. \end{aligned} \tag{15}$$

If the constant maximum motor force and speed assumption is considered, fixed operation points on the curve must be chosen, i.e., the available cable force and speed are bounded by boxes. Fig. 6 shows three scenarios of AWS and ATS of the 2-DoF planar CDPR when different operation points on the motor curve are chosen. If the point is chosen favorable to cable force (first row in Fig. 6), the AWS is large while the ATS is small. On the other hand, if this point is chosen favorable to cable speed (bottom row in Fig. 6), the ATS is large while the AWS is small. All of the above cases could only utilize a small portion of the region under the motor curve (i.e., very limited capability of the motor).

B. ATS From RWS

The W–T pair could capture the robot's actual wrench–twist available margin and, hence, efficiently utilize the hardware's capability. Using this, a new dependent ATS named the RWDATS, is proposed. It is different from the conventional zonotope ATS because its boundaries nonlinearly map from the wrench space

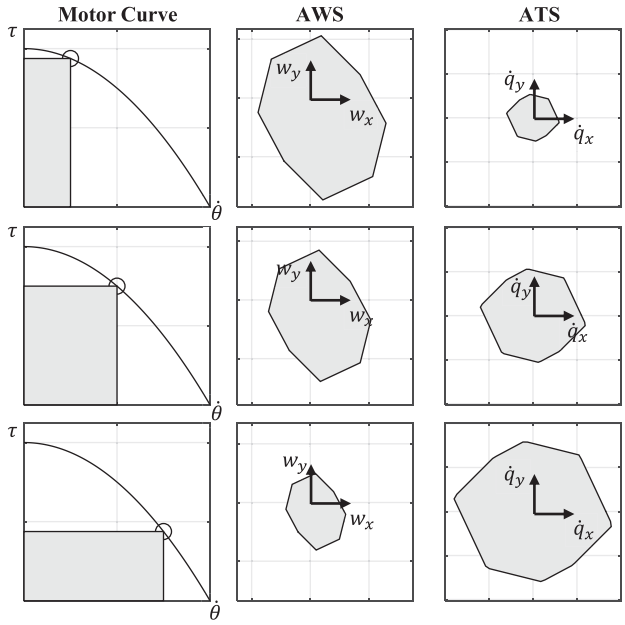

Fig. 6. Three scenarios of different motor operation points shown from top to bottom: As the cable speed $\dot{\boldsymbol{l}}$ increases, the maximum cable force $\boldsymbol{f}$ decreases. A trend that shows $\mathcal{W}_\mathrm{a}$ is shrinking while $\mathcal{T}_\mathrm{a}$ is expanding.

to the twist space. The dependent twist set can be written as

$$\mathcal{T}'_\mathrm{a}(\boldsymbol{q}, \mathcal{W}_\mathrm{r}) = \{\boldsymbol{g}(\boldsymbol{q}, \dot{\boldsymbol{l}}) \preceq \boldsymbol{0},\ \dot{\boldsymbol{l}} \in [\underline{\boldsymbol{h}}(\mathcal{W}_\mathrm{r}), \overline{\boldsymbol{h}}(\mathcal{W}_\mathrm{r})]\} \tag{16}$$

where $\boldsymbol{g}$ is a function that depends on the MP pose and cable speed. The cable speed is bounded by functions $\boldsymbol{h}$, which depend on the required wrenches.

This section would show how to map the AWS from wrench space into twist space such that the RWDATS could be obtained.

Noted that the connection between MP wrench and twist relies on the actuators' force and speed relationship. From the mathematical definition of AWS (6), the normals of the hyperplanes only depend on the MP pose as they are projections of the corresponding cable forces. The perpendicular distances of these hyperplanes also depend on the cable force bounds $\overline{\boldsymbol{f}}$.

Property 1: For a fixed pose $\boldsymbol{q}$, the perpendicular distances β depend on cable force upper bounds while the normals of hyperplanes $\boldsymbol{\alpha}$ are constants to the pose $\boldsymbol{q}$.

Consider the dot product $\beta_j(\boldsymbol{w}^\mathrm{r}) = \boldsymbol{\alpha}_j^T \boldsymbol{w}^\mathrm{r}$ where $\boldsymbol{w}^\mathrm{r} \in \mathcal{W}_\mathrm{r}$ is one of the extreme points of the RWS. The vector $\boldsymbol{\alpha}_j$ is the normal of the jth hyperplane of the AWS. The contour plot in Fig. 5 shows different values of $\boldsymbol{\alpha}_j^T \boldsymbol{w}^\mathrm{r}$ of the 2-DoF robot. The jth perpendicular distance from the origin to $\boldsymbol{w}^\mathrm{r}$, along the direction of $\boldsymbol{\alpha}_j$ is β_j.

Now consider all of the extreme points $\boldsymbol{w}^\mathrm{r}_k$. As the total number of points is finite, there exists a largest perpendicular distance β^* for each hyperplane of the AWS. It is calculated by

$$\beta_j^* = \max_{k=1,\ldots,q} \boldsymbol{\alpha}_j^T \boldsymbol{w}^\mathrm{r}_k \qquad \forall j = 1, \ldots, p. \tag{17}$$

Fig. 5 shows all values of $\boldsymbol{\alpha}_j^T \boldsymbol{w}^\mathrm{r}$ and the maximum value of β_j^*.

As stated in (7), for the robot to be wrench feasible, the perpendicular distance of the planes of the AWS, $\beta_j(\boldsymbol{q}, \overline{\boldsymbol{f}})$ must satisfy the inequality

$$\beta_j(\boldsymbol{q}, \overline{\boldsymbol{f}}) \geq \beta_j^* \ \ \forall j = 1, \ldots p. \tag{18}$$

TABLE I
NORMAL $\boldsymbol{\alpha}_j$ AND PERPENDICULAR DISTANCE β_j^* OF 2-DOF PLANAR CDPR

j	$\boldsymbol{\alpha}_j^T$	β_j^*
1	$[-0.7071, -0.7071]$	1.4142
2	$[0.4244, -0.9055]$	1.3299
3	$[0.9701, -0.2425]$	1.2127
4	$[0.8824, 0.4796]$	0.4176
5	$[0.7071, 0.7071]$	0.0000
6	$[-0.4244, 0.9055]$	1.3299
7	$[-0.9701, 0.2425]$	1.2127
8	$[-0.8824, -0.4706]$	1.3529

For the 2-DoF planar CDPR in Fig. 4 at a pose $\boldsymbol{q}_1 = [0.15,\ 0.6]^T$, the AWS is shown as the middle column of Fig. 6. It consists of eight hyperplanes. The normals and perpendicular distances corresponding to the hyperplanes can be calculated from (17), listed in Table I.

As stated in (6), the location of planes is determined by the discrete values of the wrench. Each of these wrenches is generated by different combinations of cable forces. Thus, for the jth hyperplane, the corresponding perpendicular distance β_j can be obtained by

$$\beta_j = \boldsymbol{\alpha}_j^T \boldsymbol{w} = -\boldsymbol{\alpha}_j^T \boldsymbol{J}^T \sum_{i \in \mathcal{Z}_j} \overline{f}_{i,l} \boldsymbol{e}_i \quad \forall l \tag{19}$$

with $\boldsymbol{e}_i \in \mathbb{Z}^m$ is an integer vector whose all entries are zeros except the ith entry, i.e., $\boldsymbol{e}_i = [0 \ldots 1 \ldots 0]^T$. If the maximum cable force function (15) is substituted into $\beta_j(\boldsymbol{q}, \overline{\boldsymbol{f}})$, the inequality (18) becomes

$$-\boldsymbol{\alpha}_j^T \boldsymbol{J}^T \sum_{i \in \mathcal{Z}_j} \overline{f}_{i,l} \boldsymbol{e}_i \geq \beta_j^* \quad \forall l = 1, \ldots, s. \tag{20}$$

As all piecewise segments of the motor curve are needed to fulfill the wrench requirement. Combining (20) and (17)

$$-\boldsymbol{\alpha}_j^T \boldsymbol{J}^T \sum_{i \in \mathcal{Z}_j} \overline{f}_{i,l} \boldsymbol{e}_i \geq \max_{k=1,\ldots,q} \boldsymbol{\alpha}_j^T \boldsymbol{w}^\mathrm{r}_k \quad \forall j\ \forall l. \tag{21}$$

If the cable force function (15) is expanded in terms of $\dot{l}$ and link them to MP twist space by (3), the individual maximum cable force for the ith cable and lth segment, $\overline{f}_{i,l}$ can be expressed as

$$\begin{aligned} \overline{f}_{i,l}(\dot{\boldsymbol{q}}) &= c_{i,l} \dot{l}_i^2 + b_{i,l} \dot{l}_i + a_{i,l} \\ &= c_{i,l} \boldsymbol{e}_i^T \boldsymbol{J} \dot{\boldsymbol{q}} \dot{\boldsymbol{q}}^T \boldsymbol{J}^T \boldsymbol{e}_i + b_{i,l} \boldsymbol{e}_i^T \boldsymbol{J} \dot{\boldsymbol{q}} + a_{i,l}. \end{aligned} \tag{22}$$

Substituting (22) into (21), the inequalities are now represented in MP twist space. By factorizing the terms, it could be written in a quadratic form with respect to the twist

$$\dot{\boldsymbol{q}}^T \boldsymbol{Q}_{j,l} \dot{\boldsymbol{q}} + \boldsymbol{p}_{j,l}^T \dot{\boldsymbol{q}} \leq r_{j,l} \quad \forall j \quad \forall l \tag{23}$$

where

$$\boldsymbol{Q}_{j,l}(\boldsymbol{q}) = \sum_{i \in \mathcal{Z}_j} c_{i,l} \boldsymbol{J}^T \boldsymbol{e}_i (\boldsymbol{\alpha}_j^T \boldsymbol{J}^T \boldsymbol{e}_i) \boldsymbol{e}_i^T \boldsymbol{J}$$

$$\boldsymbol{p}_{j,l}^T(\boldsymbol{q}) = \sum_{i \in \mathcal{Z}_j} b_{i,l} (\boldsymbol{\alpha}_j^T \boldsymbol{J}^T \boldsymbol{e}_i) \boldsymbol{e}_i^T \boldsymbol{J}$$

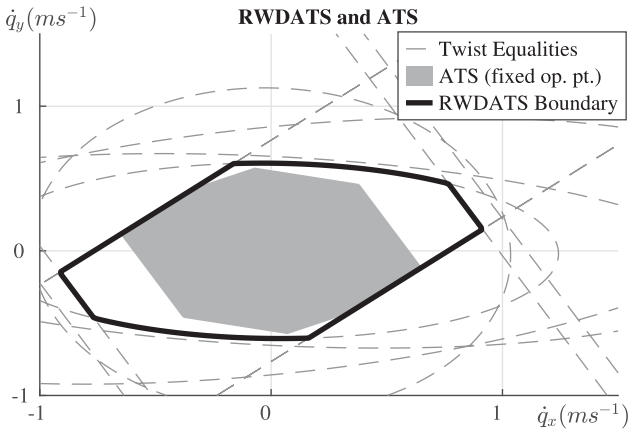

Fig. 7. All the equalities are calculated as (23) and plotted as a dotted line and the intersection of them is the RWDATS. The ATS generated under the fixed motor operation point is highlighted by the gray region for comparison.

$$r_{j,l}(\boldsymbol{q}, \mathcal{W}_\mathrm{r}) = -\boldsymbol{\alpha}_j^T \boldsymbol{J}^T \sum_{i \in \mathcal{Z}_j} a_{i,l} \boldsymbol{e}_i - \max_{k=1,\ldots,q} \boldsymbol{\alpha}_j^T \boldsymbol{w}_k^\mathrm{r}.$$

Hence, the RWDATS is the set of all twists which satisfies the inequalities (23), i.e.

$$\mathcal{T}_\mathrm{a}'(\boldsymbol{q}, \mathcal{W}_\mathrm{r}) = \{\dot{\boldsymbol{q}} \in \mathbb{R}^n : \dot{\boldsymbol{q}}^T \boldsymbol{Q}_{j,l} \dot{\boldsymbol{q}} + \boldsymbol{p}_{j,l}^T \dot{\boldsymbol{q}} \leq r_{j,l} \quad \forall j \quad \forall l\}. \tag{24}$$

To summarize, the above inequalities form a twist set that is mapped from the AWS information by the motor force–speed function. The AWS information is based on the minimal required cable force that could support the user-defined RWS. The following list briefly describes the procedure for how to obtain the RWATS at a particular MP pose.

1) Obtain all normal vector $\boldsymbol{\alpha}_j$ of the jth bounding plane of the AWS.
2) For each plane, calculate the distances between the origin and convex RWS by taking the maximum value among all vertices of the RWS.
3) This distance β_j^* ensures that the entire RWS is below the plane of the AWS.
4) The distance is shifted by the contributing cable force, which is bounded by the quadratic functions.
5) A set of inequalities is formed by setting the shifted distance larger or equal to β_j^*.

Suppose all the motor curves of the mentioned 2-DoF CDPR are equal, equated as a quadratic equation (15), with $a = -2$, $b = 0$, $c = -2$, and $l = 1$. With the perpendicular distance β^* from Table I and the equalities (23), all wrench-dependent twist boundaries are plotted in Fig. 7. The intersection of the inequalities (the region highlighted by the black bold line) is the RWDATS.

For comparison, the ATS generated from the fixed operating point will be calculated. The largest possible ATS is generated by the highest available cable speed bounds. Since the cable speed is inversely related to the cable force, the highest possible cable speed is achieved by using the least possible cable force. The minimum required cable forces upper bound $\overline{\boldsymbol{f}}$ to perform each required wrench can be found by linear programming

$$\begin{aligned} \overline{\boldsymbol{f}} = \underset{\boldsymbol{f}}{\operatorname{argmin}} \quad & \|\boldsymbol{f}\|_\infty \\ \text{s.t.} \quad & \boldsymbol{w}_k^\mathrm{r} = -\boldsymbol{J}^T \boldsymbol{f}. \end{aligned} \tag{25}$$

It would minimize the infinite norm of the cable force such that the largest individual cable force is at the minimum. To ensure that the cable force could perform all required wrench, the maximum value $\max(\operatorname{argmin} \|\boldsymbol{f}\|_\infty)$ is taken. The maximum available cable speed is obtained from the motor curve. In this example, the maximum allowable cable speed is 0.5412.

In Fig. 7, a conventional twist set is generated by using fixed cable speed. It can be seen that ATS (fixed cable speed bound) is a subset of the dependent twist set. All ATSs generated by the fixed operating point method are always the subsets of corresponding RWDATSs, regardless of how the cable forces are selected.

IV. WTFW and Maximum Available Twist Ball

In this section, a workspace condition based on the simultaneous feasibility is presented to show the improvement of the feasible region, and a workspace metric to quantify the MP performance in terms of maximum allowable twist value.

A. Wrench–Twist Feasible Condition and Workspace

A pose in the operational space fulfills the wrench–twist feasible condition if and only if the RTS is a subset of the RWDATS. Furthermore, if both of the twist sets are convex, one could only check whether the extreme points of the RTS satisfy the inequalities in (23). The RTS could be set to be convex as it is a user-defined set. The convexity of the RWDATS would be proven in the following.

Lemma 1: The matrix $\boldsymbol{Q}_{j,l}$ in (23) is positive semidefinite if the lth segment of the motor curve is represented by a concave quadratic function.

Proof: For any given i and j, the expression $c_{i,l} \boldsymbol{J}^T \boldsymbol{e}_i (\boldsymbol{\alpha}_j^T \boldsymbol{J}^T \boldsymbol{e}_i) \boldsymbol{e}_i^T \boldsymbol{J}$ could be expressed as $d_{i,l} \boldsymbol{J}^T \boldsymbol{e}_i (\boldsymbol{J}^T \boldsymbol{e}_i)^T$, where $d_{i,l} = c_{i,l} (\boldsymbol{\alpha}_j^T \boldsymbol{J}^T \boldsymbol{e}_i) \in \mathbb{R}$. Noted that a matrix multiplied by its transpose is always positive semidefinite. From the work in [28], the shifting wrenches $(-\boldsymbol{J}^T \boldsymbol{e}_i)$ are in the same half-space with the normal of the hyperplane $(\boldsymbol{\alpha}_j)$. Hence, $(\boldsymbol{\alpha}_j^T \boldsymbol{J}^T \boldsymbol{e}_i) \leq 0$. As the motor curve is concave downward, $c_{i,l} \leq 0$. Therefore, matrix $c_{i,l} \boldsymbol{J}^T \boldsymbol{e}_i (\boldsymbol{\alpha}_j^T \boldsymbol{J}^T \boldsymbol{e}_i) \boldsymbol{e}_i^T \boldsymbol{J}$ is positive semidefinite. Finally, $\boldsymbol{Q}_{j,l}$ is also positive semidefinite as it is the sum of all positive semidefinite matrices. ■

Theorem 1: If the motor curve is represented by a combination of linear and concave quadratic functions, the RWDATSs are convex regardless of the pose of the MP and the RWS.

Proof: Equation (23) is linear and the corresponding bounded set is convex if the lth segment of the motor curve is represented by a linear function. The set bounded by (23) is also convex if the $\boldsymbol{Q}_{j,l}$ term in the lth segment of the quadratic motor curve is positive semidefinite. As the RWDATS is an intersection of all the convex sets, it is also convex. ■

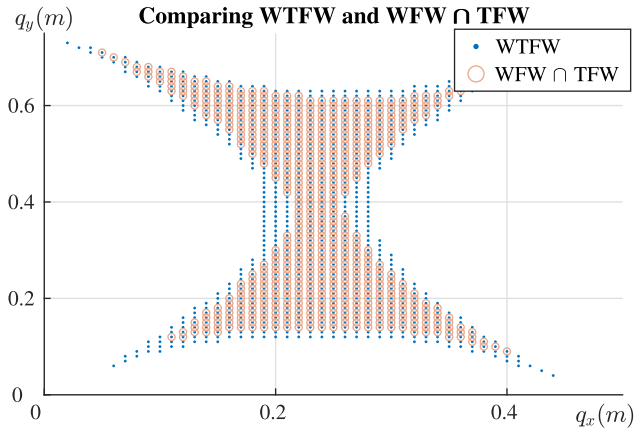

Fig. 8. Intersection of TFW and WFW is compared with the WTFW of a 2-DoF CDPR.

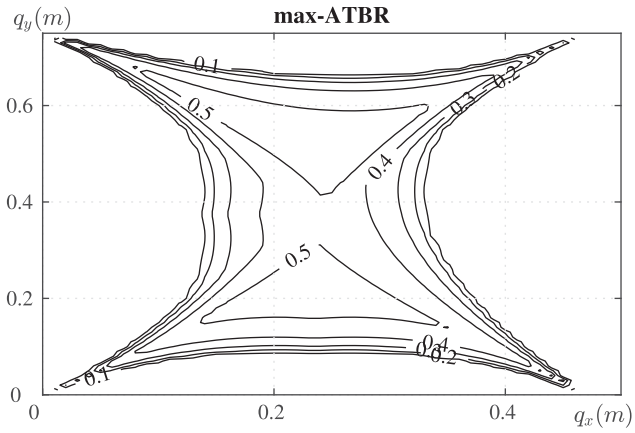

Fig. 9. Max-ATBR of a 2-DoF CDPR.

The WTFW is a set of poses that fulfill the wrench–twist feasible condition. Mathematically, it is defined as

$$\text{WTFW} = \{\boldsymbol{q} : \ \mathcal{T}_\text{r} \subseteq \mathcal{T}'_\text{a}(\boldsymbol{q}, \mathcal{W}_\text{r})\}. \tag{26}$$

Suppose the RTS of the planar cable robot is a box, with corners $\{(-0.3, -0.3), (-0.3, 0.3), (0.3, -0.3), (0.3, 0.3)\}$. Using the RWDATS approach, the WTFW is shown in Fig. 8. For comparison, the TFW and the WFW are also generated using fix operating point assumption. The upper bounds of cable speed and force are picked within the motor curve by the same method stated in (25), they are $\overline{\dot{l}} = 0.45$ and $\overline{f} = 1.595$. With this operation point, AWS and ATS at different MP poses are generated and the feasibility condition is checked separately by (7) and (11), respectively. The intersection of WFW and TFW represents the simultaneous feasible workspace, in which both wrench and twist are feasible. The intersected workspace is physically smaller than the WTFW.

B. Maximum Available Twist Ball Radius

The following section includes a new type of workspace metric applicable for the WTFW, the *maximum available twist ball radius* (Max-ATBR). It is particularly useful when the user has no special requirement for the twist. It indicates the radius of the inscribed twist ball of the RWDATS (second-norm of twist, $\|\dot{\boldsymbol{q}}^*\|(\boldsymbol{q}, \mathcal{W}_\text{r})$). It is the minimum possible speed of the MP in all directions at a specific pose. The motors can generate enough torque and speed for the MP as long as the magnitude of the required twist is least than this value. Hence, the max-ATBR can be a reference speed that the user can assign to it the MP. Mathematically, the above statement can be expressed as

$$\|\dot{\boldsymbol{q}}\| \leq \|\dot{\boldsymbol{q}}^*\| \rightarrow \dot{\boldsymbol{q}} \in \mathcal{T}_\text{a}. \tag{27}$$

Consider the quadratic boundary of the RWDATS, (23), it could be represented as

$$g_{j,l}(\dot{\boldsymbol{q}}_{j,l}) = \dot{\boldsymbol{q}}_{j,l}^T \boldsymbol{Q}_{j,l} \dot{\boldsymbol{q}}_{j,l} + \boldsymbol{p}_{j,l}^T \dot{\boldsymbol{q}}_{j,l} - r_{j,l} = 0. \tag{28}$$

As the angular velocity and the linear velocity could not be compared directly. Two independent twist balls are founded separately. Note that the twist of the CDPR could be partitioned as $\boldsymbol{q} = [\dot{\boldsymbol{q}}_p^T \ \ \dot{\boldsymbol{q}}_r^T]^T$, where $\dot{\boldsymbol{q}}_p$ is the linear velocity and $\dot{\boldsymbol{q}}_r$ is the angular velocity. Then, the $\boldsymbol{Q}_{j,l}$ and $\boldsymbol{p}_{j,l}$ can be partitioned as

$$\boldsymbol{Q} = \begin{bmatrix} \boldsymbol{Q}_{pp} & \boldsymbol{Q}_{pr} \\ \boldsymbol{Q}_{rp} & \boldsymbol{Q}_{rr} \end{bmatrix}, \quad \boldsymbol{p} = \begin{bmatrix} \boldsymbol{p}_p \\ \boldsymbol{p}_r \end{bmatrix} \tag{29}$$

for all j, l. The subscriptions are dropped for clarity. If linear and angular velocities are decoupled, the equality (28) becomes two equations

$$g_p(\dot{\boldsymbol{q}}_p) = \dot{\boldsymbol{q}}_p^T \boldsymbol{Q}_{pp} \dot{\boldsymbol{q}}_p + \boldsymbol{p}_p^T \dot{\boldsymbol{q}}_p - r = 0 \tag{30}$$

$$g_r(\dot{\boldsymbol{q}}_r) = \dot{\boldsymbol{q}}_r^T \boldsymbol{Q}_{rr} \dot{\boldsymbol{q}}_r + \boldsymbol{p}_r^T \dot{\boldsymbol{q}}_r - r = 0. \tag{31}$$

According to the work in [31], if $\dot{\boldsymbol{q}}_{j,l}^*$ on the surface is the closest point to the origin, then it is also normal to the surface. By using the fact that the gradient $\nabla g_{j,l}(\dot{\boldsymbol{q}}_{j,l})$ is normal to the surface, $\dot{\boldsymbol{q}}_{j,l}^*$ must satisfy

$$\dot{\boldsymbol{q}}_{j,l}^* = -\lambda \nabla g_{j,l}(\dot{\boldsymbol{q}}_{j,l}^*) = \lambda(2\boldsymbol{Q}_{j,l}\dot{\boldsymbol{q}}_{j,l}^* + \boldsymbol{p}_{j,l}) \tag{32}$$

and hence

$$\dot{\boldsymbol{q}}_{j,l}^* = -\lambda(\boldsymbol{I} + 2\lambda \boldsymbol{Q}_{j,l})^{-1} \boldsymbol{p}_{j,l} \tag{33}$$

with some constant λ representing the perpendicular distance. Solving for $\dot{\boldsymbol{q}}_{j,l}^*$ would return all the points on the surface that is perpendicular to it. By substituting the $\dot{\boldsymbol{q}}_{j,l}^*$ from (33) into (28), a polynomial in terms of λ is obtained. The shortest length among all of the solutions represents the shortest distance between the origin and the surface $g_{j,l}$. The max-ATBR, $\dot{q}^* \in \mathbb{R}$, is the smallest magnitude of all $\dot{\boldsymbol{q}}_{j,l}^*$, and hence

$$\dot{q}^* = \min_{j,l} \ \|\dot{\boldsymbol{q}}_{j,l}^*\|. \tag{34}$$

For instance, the max-ATBR of the 2-DoF planar CDPR of interest at $\boldsymbol{q}_1 = [0.15, \ 0.6]^T$ is 0.5412. By evaluating the whole workspace, a distribution of max-ATBR can be compared (shown in Fig. 9). Noticed that when max-ATBR $= 0$, it indicates the boundary of a special WTFW that the twist requirement is an empty set, $\mathcal{T}_\text{r} = \emptyset$. It is equivalent to the WFW when the operation point is chosen to be the stall torque on the motor curve.

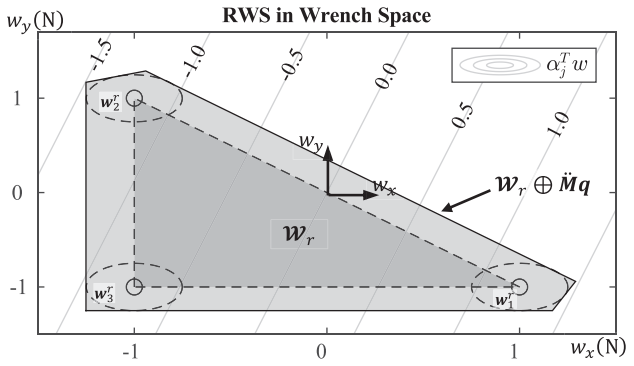

Fig. 10. RWS is a polygon that includes the Minkowski sum of the triangular RWS and the wrench ball of acceleration.

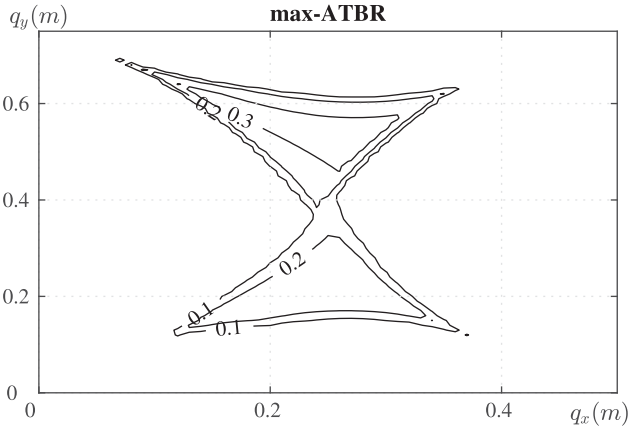

Fig. 11. Contour plot of the max-ATBR. The RWS includes acceleration capability. Hence, the overall value is decreased.

The max-ATBR defined above should have at least acceleration continuity to allow the MP to alter its speed from one point to another within the workspace. Discretizing the workspace in a pointwise manner, it can be assumed that the MP only accelerates along the discretizing axes of the workspace. The possible maximum acceleration between two points, such as from A and B, can be approximated by

$$\ddot{\boldsymbol{q}}(\boldsymbol{q}_A, \boldsymbol{q}_B) \leq \frac{\|\dot{\boldsymbol{q}}_A^*\|^2 + \|\dot{\boldsymbol{q}}_B^*\|^2}{2\|\boldsymbol{q}_B - \boldsymbol{q}_A\|^2}(\boldsymbol{q}_B - \boldsymbol{q}_A) \tag{35}$$

where $\leq$ here means elementwise least than or equal to. It is because the $\|\dot{\boldsymbol{q}}_A^*\|^2 + \|\dot{\boldsymbol{q}}_B^*\|^2$ is the speed difference of the two poses running in the opposite direction. It can be seen that the acceleration would introduce a dependence between MP poses. A conservative approach is to consider an acceleration upper bound $\overline{\|\ddot{\boldsymbol{q}}\|}$ such that it satisfies the condition

$$\|\ddot{\boldsymbol{q}}(\boldsymbol{q}_A, \boldsymbol{q}_B)\| \leq \overline{\|\ddot{\boldsymbol{q}}\|}, \ \forall \boldsymbol{q}_B \in \mathcal{N}(\boldsymbol{q}_A) \quad \forall \boldsymbol{q}_A \in \text{WFW} \tag{36}$$

where $\mathcal{N}(\boldsymbol{q}_A)$ is the set that contains all poses adjacent to $\boldsymbol{q}_A$. It can be added to the RWS by $\mathcal{W}_\text{r} \oplus \boldsymbol{M}(\boldsymbol{q})\ddot{\boldsymbol{q}}$, where $\oplus$ is the Minkowski sum of two sets. Again, as the linear and angular velocities should not be directly compared, two acceleration bounds should be set to different values.

The following list briefly describes the procedure for how to obtain the max-ATBR.

1) Change the inequalities in (24) into equalities.
2) Find the minimum distance between each quadratic surface and the origin.
3) The max-ATBR would be the smallest value of these distances.

If acceleration is explicitly considered, then the following holds.

4) With all max-ATBR, the acceleration from one pose to another could be approximated.
5) Include the MP acceleration as part of the RWS and run the max-ATBR again.

Suppose the 2-DoF MP weights 0.5 kg and $\overline{\|\ddot{\boldsymbol{q}}\|} = 0.5\ \text{ms}^{-2}$, the new RWS is shown in Fig. 10. It is a polygon that includes the RWS formed by doing a Minkowski sum of the triangular RWS as defined in Fig. 5 and a wrench ball of acceleration, resulting in a convex polygon with five vertices. Fig. 11 shows the overall speed decreases to increase wrench capability in order to perform the required acceleration.

C. Direction-Dependent RWDATS

It should be noted that the max-ATBR is a conservative measure of speed because it guarantees the MP to perform the same amount of twists in all directions. The actual speed to a specific direction must be greater than or equal to max-ATBR. The directional maximum available twist (DAT) is obtained from the inequalities stated in (23) once they are available from workspace generation. However, in high dimensions, it is impractical to store the whole twist set at each workspace point. The authors propose the discretized directional maximum ATS (DDATS), which stores only a limited number of DAT. These are the directions that are pointing from the current workspace point to all other adjacent points. Each DAT can be calculated by the following modified equation from (22):

$$\overline{f}_{i,l}(\dot{\boldsymbol{q}}) = c_{i,l}\boldsymbol{e}_i^T\boldsymbol{J}\|\dot{\boldsymbol{q}}\|^2\hat{\boldsymbol{q}}\hat{\boldsymbol{q}}^T\boldsymbol{J}^T\boldsymbol{e}_i + b_{i,l}\boldsymbol{e}_i^T\boldsymbol{J}\|\dot{\boldsymbol{q}}\|\hat{\boldsymbol{q}} + a_{i,l} \tag{37}$$

with $\hat{\boldsymbol{q}}$ is a unit vector indicating the prescribed twist direction. Substituting (37) into (21), it becomes a quadratic inequality similar to (23) with one scalar variable $\|\dot{\boldsymbol{q}}\|_2$

$$Q_{j,l}\|\dot{\boldsymbol{q}}\|^2 + p_{j,l}\|\dot{\boldsymbol{q}}\| \leq r_{j,l} \quad \forall j \quad \forall l \tag{38}$$

where

$$Q_{j,l} = \boldsymbol{\alpha}_j^T\boldsymbol{J}^T\sum_{i\in\mathcal{Z}_j} c_{i,l}\hat{\boldsymbol{q}}^T\boldsymbol{J}^T\boldsymbol{e}_i\boldsymbol{e}_i^T\boldsymbol{J}\hat{\boldsymbol{q}}\boldsymbol{e}_i$$

$$p_{j,l}^T = \boldsymbol{\alpha}_j^T\boldsymbol{J}^T\sum_{i\in\mathcal{Z}_j} b_{i,l}\boldsymbol{e}_i^T\boldsymbol{J}\hat{\boldsymbol{q}}\boldsymbol{e}_i$$

$$r_{j,l} = -\boldsymbol{\alpha}_j^T\boldsymbol{J}^T\sum_{i\in\mathcal{Z}_j} a_{i,l}\boldsymbol{e}_i - \max_{k=1,\ldots,q}\boldsymbol{\alpha}_j^T\boldsymbol{w}_k^\text{r}.$$

A solution to the above is the maximum available speed along the direction $\hat{\boldsymbol{q}}$, i.e.

$$\text{DAT}(\hat{\boldsymbol{q}}, \boldsymbol{q}) = \hat{\boldsymbol{q}}\min_{j,l}(\|\dot{\boldsymbol{q}}_{j,l}\|) = \hat{\boldsymbol{q}}\dot{q}_r^* \tag{39}$$

where $q_r^* = \min(\|\dot{\boldsymbol{q}}_{j,l}\|) \in \mathbb{R}$ represents the magnitude of speed with the given direction and $\dot{\boldsymbol{q}}_{j,l}$ satisfies

$$Q_{j,l}(\hat{\boldsymbol{q}}, \boldsymbol{q})\|\dot{\boldsymbol{q}}_{j,l}\|^2 + p_{j,l}(\hat{\boldsymbol{q}}, \boldsymbol{q})\|\dot{\boldsymbol{q}}_{j,l}\| = r_{j,l} \quad \forall j \quad \forall l. \tag{40}$$

The positive and negative roots represent two solutions in positive $\hat{\boldsymbol{q}}$ and opposite $\hat{\boldsymbol{q}}$ direction, respectively. Thus, the twist sets can be stored as a collection of maximum available speed in discretized directions. This set can be expressed as

$$\text{DDATS} = \Big\{\dot{\boldsymbol{q}} : \text{DAT}(\hat{\boldsymbol{q}}, \boldsymbol{q}_A),\ \hat{\boldsymbol{q}} = \frac{\boldsymbol{q}_B - \boldsymbol{q}_A}{\|\boldsymbol{q}_B - \boldsymbol{q}_A\|} \quad \forall \boldsymbol{q}_B \in \mathcal{N}(\boldsymbol{q}_A) \quad \forall \boldsymbol{q}_A \in \text{WFW}\Big\}. \tag{41}$$

The discretized max speed values can be used in trajectory planning presented in the next section and provide a reasonable simplification of saving the collection of twist sets of the whole workspace.

V. Time Optimal Trajectory Generation

This section demonstrates the use of the coupled motor torque–speed relationship in MP trajectory planning by making use of the metrics. It has two steps, first, it starts from a weighted graph, which is generated by the max-ATBR or discretized RWDATS metric. An optimal EE moving path (in terms of least traveling time) can be searched from the graph. Second, it processes the resulting path by smoothing, increasing its resolution, and re-evaluating the maximum possible twist along the path. By assigning the twist to the path, the time vector is obtained and the trajectory is planned.

A. Time Optimal Path Searching in the Max Twist Map

With the aid of the pregenerated workspace with the maximum possible twist value, a time-optimal path could be searched by the Dijkstra algorithm. The cost (the traveling time) on an edge of the graph connecting two nodes i and j is calculated by

$$f_{i,j} = \begin{cases} \frac{\|\boldsymbol{q}_i^2 - \boldsymbol{q}_j^2\|_2}{2}\left(\frac{1}{\dot{q}_i^*} + \frac{1}{\dot{q}_j^*}\right) & \text{max-ATBR} \\ \frac{\|\boldsymbol{q}_i^2 - \boldsymbol{q}_j^2\|_2}{2}\left(\frac{1}{(\dot{q}_r^*)_i} + \frac{1}{(\dot{q}_r^*)_j}\right) & \text{DDAT} \end{cases} \tag{42}$$

where $\dot{q}^*$ and $\dot{q}_r^*$ are the values of max-ATBR [as in (34)] and DAT pointing at $\hat{\boldsymbol{q}}$ direction [as in (39)] respectively.

As mentioned in Section IV-C, max-ATBR is a conservative metric since it is the largest inscribed ball of the twist set. Therefore, planning on a DDAT map usually could provide a better trajectory than using max-ATBR. However, the computational time for calculating a max-ATBR metric is faster than DDAT. Using the same 2-DoF CDPR and motor set as an example, multiple start-end point pairs were simulated. One of the pairs is shown in Fig. 12. Table II compares the difference in path planning using two metrics. It compares the computational time of generating the metrics. Different paths are searched from the randomly selected start and endpoints, and the mean time of optimal path searching and the returned cost of the Dijkstra algorithm are also written. There is a trend that the DDAT metric provides a better cost yet requires more time to search and generate the workspace.

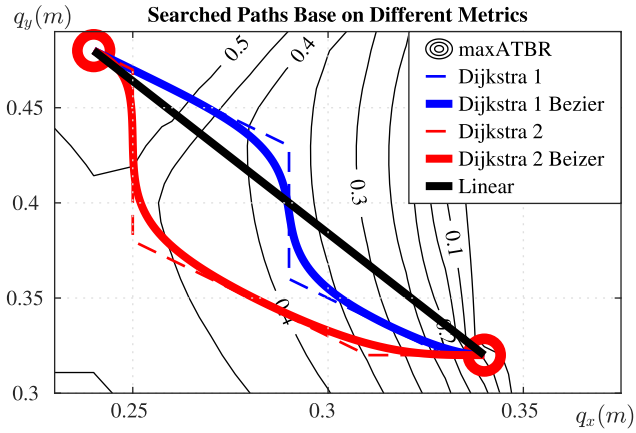

Fig. 12. Comparison of found paths using max-ATBR (Dijkstra 1), DDAT (Dijkstra 2), and linear path. Solid lines are corresponding Bezier smoothed curves.

TABLE II
Mean Value of Path Search Time and Path Total Cost

	Max-ATBR	DDAT
Graph Generation Time	13.23s	57.37s
Path Search Time (Mean)	1.65s	1.83s
Path Total Cost (Mean)	0.63s	0.59s

B. Refinement of the Time-Optimal Path and the Time-Optimal Trajectory

The identified path from the above subsection is usually coarse because it is generated from a coarse workspace grid. To improve the smoothness of the path, it is interpolated as a Bezier curve. Suppose the path now has n_p steps after smoothing, the re-evaluation process will begin from the end pose to the start pose of the path, as stated in Algorithm 1.

It is assumed that the MP stops at zero twist, i.e., $\|\dot{\boldsymbol{q}}_{n_p}\| = \boldsymbol{0}$. The total time that the MP requires to travel from the start point to the endpoint equals Σt_i. In summary, by picking an appropriate twist, one can minimize the total traveling time of the MP of a specified path.

Fig. 12 shows different path-planning strategies on a magnified max-ATBR plot. After re-evaluating, the magnitude of the MP twist varies at different steps of the path. To compare, the twist verse traveling time of different trajectories is plotted in Fig. 13. The fixed twist of the linear trajectory (*Linear 2* in Fig. 13) must be the lowest. Since that twist must be available everywhere along the path. As one of the endpoints locates at the boundary of the workspace, that fixed twist is low valued. Even if the path-searching algorithm is not applied, given the linear trajectory, one can still evaluate the varying twist by DAT and a significant time difference with linear trajectory is shown (*Linear 1* in Fig. 13). The total traveling time of these trajectories (from fastest to slowest) is 0.45, 0.53, 0.61, and 1.76 s.

Algorithm 1: Algorithm for Obtaining the Time Vector of A Prescribed Path.

Require: Pose along the prescribed path $\boldsymbol{q}_i,\ i = \{1 \ldots n_p\}$;
Ensure: Time vector $\boldsymbol{t}$
Initialization: $\dot{\boldsymbol{q}} \leftarrow \boldsymbol{0}$, acceleration error ϵ

```
for i = n_p − 1 to 1 do
    a_i ← 0  % temporary acceleration
    while true do
        W_r ← w^r ⊕ a_i  % include acceleration by Minkowski addition
        q̇_i ← DAT(W_r, q_i)
        t_i ← q̇_i / ‖q_{i+1} − q_i‖_2  % approximated traveling time
        q̈_i ← (q̇_{i+1} − q̇_i) / t_i  % actual acceleration between two points
        if ‖q̈_i − a_i‖_2 < ϵ then
            break
        else
            a_i ← q̈_i % use the actual acceleration in next iteration
        end if
    end while
end for
return t
```

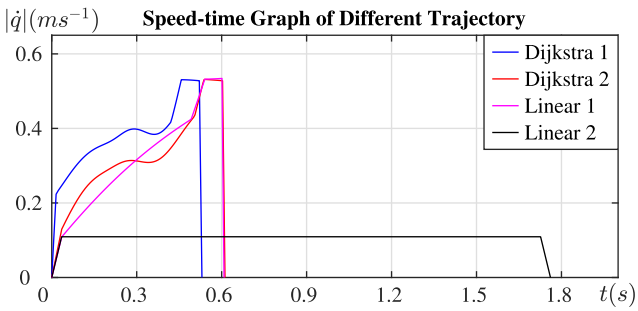

Fig. 13. Twist-time plot for comparing different trajectories. Dijkstra 1 and 2 are searched from max-ATBD and DDAT, respectively. Linear 1 is a linear path trajectory with a varying twist along the path. Linear 2 is a linear trajectory with a constant twist (max. fixed twist).

VI. 6-DoF CDPR Example

This section illustrates how the mentioned methodology in previous sections is also applicable to higher DoF CDPRs. The robot setup is listed as follows: The MP is an extruded trapezium with a height of 0.131 m, a short base length of 0.123 m, and a long base length of 0.23 m. It has an extruded thickness of 0.23 m. It has a 6-DoF task space (i.e., $\boldsymbol{q} \in \mathbb{R}^6$). It is attached by eight cables, to a cuboid frame with dimension $4 \times 4 \times 4 \times 2.5\text{m}^3$. The setup is shown in Fig. 14. The same motor curves ($f = -2\dot{l}^2 + 2$) would be applied to this robot.

A. WTFW and Max-ATBR of the 6-DoF CDPR

Suppose the gravity is aligned with the negative q_3 axis and it is always present as -0.1N. The required wrench is listed as follows:

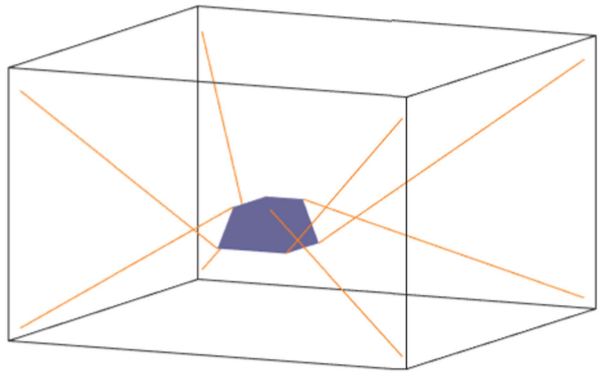

Fig. 14. Setup of the 6-DoF CDPR.

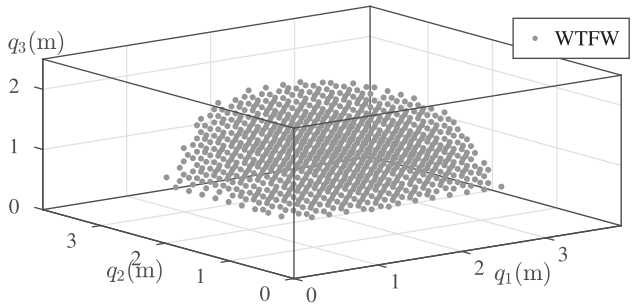

Fig. 15. WTFW of a 6-DoF, 8 cables CDPR. The orientation is fixed at 0 ($\boldsymbol{q}_4 = \boldsymbol{q}_5 = \boldsymbol{q}_6 = \boldsymbol{0}$).

$$\mathcal{W}_\text{r}: \left\{ \forall \boldsymbol{w} \quad \begin{vmatrix} w_1, w_2 \in [-0.10,\ 0.10] \\ w_4, w_5 \in [-0.05,\ 0.05] \\ w_3 \in [-0.2,\ 0], \quad w_6 = 0 \end{vmatrix} \right. \tag{43}$$

which is an offset 5-D box in 6-D wrench space. The RTS in this example is

$$\mathcal{T}_\text{r}: \left\{ \forall \boldsymbol{w} \quad \begin{vmatrix} w_1, w_2 \in [-0.20,\ 0.20] \\ w_4, w_5 \in [-0.10,\ 0.10] \\ w_3 \in [-0.4,\ 0], \quad w_6 = 0 \end{vmatrix} \right. . \tag{44}$$

It is another 5-D box in twist space. Two sets of poses are chosen to plot the WTFW. For the first set, the rotation is fixed at $\boldsymbol{0}$, i.e., $\boldsymbol{q} = [q_1,\ q_2,\ q_3,\ 0,\ 0,\ 0]^T$. With a grid of $[20,\ 20,\ 11]$ steps along q_1, q_2, q_3 axes, respectively, 4400 points in space are evaluated. Fig. 15 shows the workspace of the CDPR in q_1, q_2, q_3 axes. The intersection of traditional WFW and TFW provides the actual operational workspace of the CDPR. For the sake of comparison, three fixed maximum motor torque–speed pairs are chosen as $(\overline{f}, \overline{\dot{l}}) = (1.60, 0.45), (1.55, 0.475), (1.50, 0.5)$. The corresponding WFW and TFW pairs are plotted in Fig. 16. The detailed linear intersect feasible workspace volume to WTFW (red regions compare to WTFW in Fig. 15) ratio are shown in Table III. From the volume ratio, the intersected workspace is always smaller than the WTFW. The smallest volume difference occurs at $(\overline{f}, \overline{\dot{l}}) = (1.50, 0.5)$.

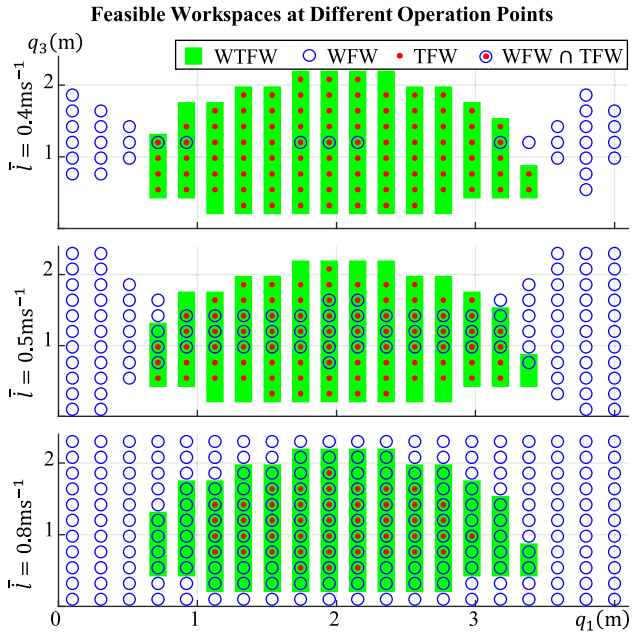

Fig. 16. Linear WFWs and TFWs and their intersections. From left to right, these figures represent the workspaces with a decreasing $\bar{f}$ (thus increasing $\bar{l}$) trend. The volume of WFW decreases from left to right but the volume of TFW increases.

TABLE III
TRADITIONAL INTERSECT FEASIBLE WORKSPACE TO WTFW VOLUME RATIO

$(\bar{f}, \bar{l})$	$V_{\cap,t}/V_{WTFW}$	$V_{\cap,r}/V_{WTFW}$
(1.60, 0.45)	0.02	17.2
(1.550.48)	20.5	92.1
(1.500.50)	70.7	70.0

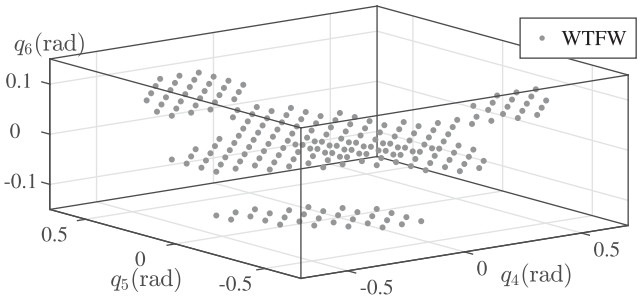

Fig. 17. WTFW at a fixed position of $[2.0,\ 1.0,\ 1.5]^T$.

The second set of poses is chosen to be at some fixed point in linear space, i.e., $\boldsymbol{q} = [2.0, 1.0, 1.15, q_4, q_5, q_6]^T$. With a discretization grid [20,20,5] steps along q_4, q_5, q_6 axes, 2000 points are evaluated. The boundaries of orientation coordinates are found by wrench closure condition, and they are

$$\begin{aligned} -\pi/4 \le q_4 \le \pi/4 \\ -\pi/4 \le q_5 \le \pi/4 \\ -\pi/18 \le q_6 \le \pi/18. \end{aligned} \tag{45}$$

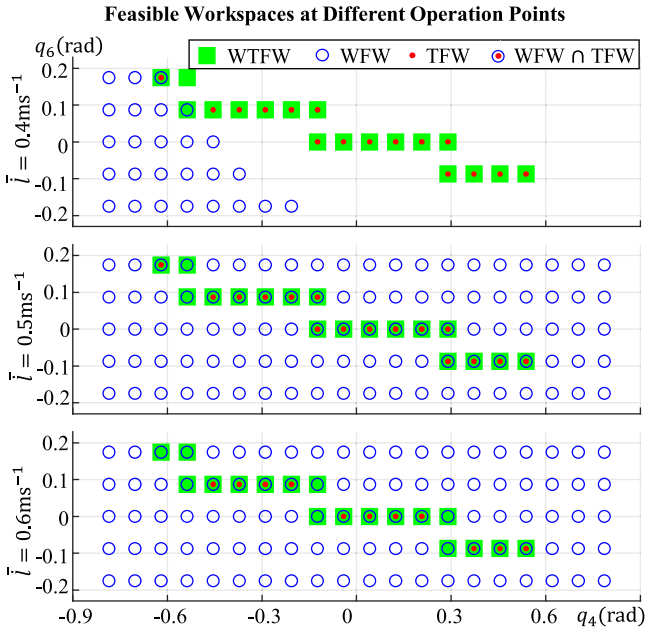

Fig. 18. Rotational WFWs and TFWs and their intersections. $\bar{f}, \bar{l}$ trends are the same as Fig. 16.

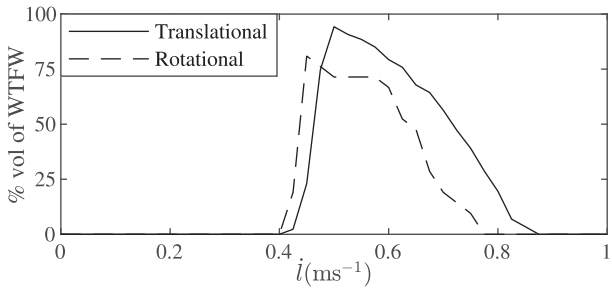

Fig. 19. Volumes intersection of WFW and TFW generated from different fixed cable force and speed are compared to the volume of WTFW.

The angular WTFW is plotted in Fig. 17. To compare the angular WTFW with the intersect workspaces, three more fixed maximum motor torque-speed pairs are chosen as $(\bar{f}, \bar{l}) = (1.60, 0.4), (1.50, 0.5), (1.28, 0.6)$. Fig. 18 depicts the corresponding WFW and TFW pairs. The intersect workspace volume to WTFW ratios are also shown in Table III. From the volume ratio, the intersected workspace is always smaller than the WTFW. The smallest volume difference occurs at $(\bar{f}, \bar{l}) = (1.550, 0.48)$. Noted that two maximums occur at different torque–speed pairs. Therefore, for the 6-D volume ratio, the least volume difference would be even larger.

A more comprehensive comparison (see Fig. 19) shows the volume difference between the two methods in the linear and angular workspace, separately. Two fixed poses are chosen as $[q_1,\ q_2,\ q_3,\ 0,\ 0,\ 0]$ and $[2,\ 2,\ 1.1,\ q_4,\ q_5,\ q_6]$. The largest intersected workspace volume of the linear and angular workspace is 94% and 81%, respectively. It is showing that any fixed motor torque–speed pair generated intersected workspaces (WFW ∩ TFW) are always a subset of the WTFW.

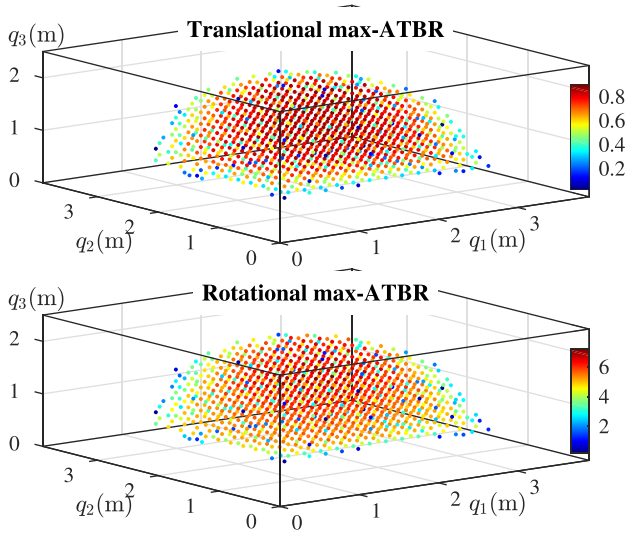

Fig. 20. Distribution max-ATBR showing in translational space, with the MP is always fixed at **0** orientation. The upper figure is the linear max-ATBR and the lower figure is the angular max-ATBR.

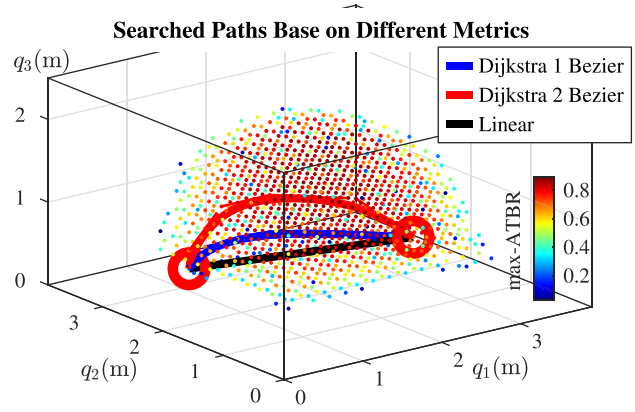

Fig. 21. Comparison of the found path using max-ATBR (Dijkstra 1) and DDAT (Dijkstra 2).

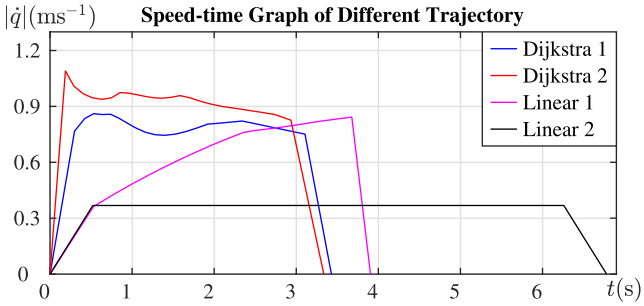

Fig. 22. Speed–time plot for comparing different trajectories of the 6-DoF CDPR. Dijkstra 1 and 2 are searched from max-ATBD and DDAT, respectively. Linear 1 is a linear path trajectory with a varying twist along the path. Linear 2 is a linear trajectory with a constant twist (max. fixed twist).

If the RTS is not specified, one could again use max-ATBR or DDAT to realize the maximum possible twist. As the DoF of this robot is separated into linear and angular, this analysis should also be done separately. Hence, two independent twist balls can be found using (34). As shown in Fig. 20, the max-ATBR is plotted as different colors of the dots, and the orientation of the MP is again held at **0**. It is expected that the max-ATBR is longer in the center part of the workspace as there is farther apart from the singularity of the CDPR. The linear and angular velocities are decoupled into two sets of 3-D balls because the magnitudes of linear and angular velocities cannot be compared directly. Hence, the MP would not perform two types of velocity simultaneously.

B. Path Searching and Trajectory Generation

Two points in the WTFW are picked to be searched for a time-optimal path. It starts at $[0.9,\ 2.7,\ 0.32,\ 0,\ 0,\ 0]^T$ and ends at $[3,\ 1.7,\ 0.5,\ 0,\ 0,\ 0]^T$. Again, two paths are searched by the Dijkstra algorithm with different cost maps and a linear path is plotted for comparison. As the rotation is kept at constant **0**, the max-ATBR map shown in the upper subplot of Fig. 20 is used. The resulting paths are shown in Fig. 21. The corresponding twist–time curve is shown in Fig. 22. The total traveling time of these trajectories (from fastest to slowest) is 3.25, 3.43, 3.90, and 6.78 s.

Ten additional paths are tested based on the random sets of start and end points. The mean traveling time of the trajectories is listed in Table IV. The ratio shows the effectiveness of considering a varying speed trajectory. Even if the metrics are not evaluated, a linear path with varying twist trajectory still has a significant improvement with a 42% decrease in total traveling time. It also shows that the trajectories generated from a DDAT map are slightly more time-efficient than using max-ATBR. However, the time for obtaining the DDAT graph and DDAT

TABLE IV
MEAN VALUE OF PATH TRAVELING TIME AND RATIO TO LINEAR TRAJECTORY

	Mean Path Searching Time	Ratio to Lin. Traj.
Max-ATBR	2.40s	0.51
DDAT	2.31s	0.49
Lin. Path, Var. $\dot{q}$	2.57s	0.58
Lin. Traj.	4.87s	/

TABLE V
MEAN VALUE AND THE RATIO OF COMPUTATIONAL TIME OF PATH SEARCH AND METRIC EVALUATION

	Path Search	Metric Evaluatio
Max-ATBR	3.03s	1022s
DDAT	3.57s	13228s

trajectory is usually longer than max-ATBR. Table V compares the computational time for generating the new path and metric maps of these two methods. In terms of path searching time, the max-ATBR requires 15.1% less computational time than the DDAT. In terms of metrics generation, the max-ATBR requires 92.3% less computational time than the DDAT.

VII. EXPERIMENT

This section shows that the proposed methodology is applied to a hardware example. A 6-DoF CDPR is designed for

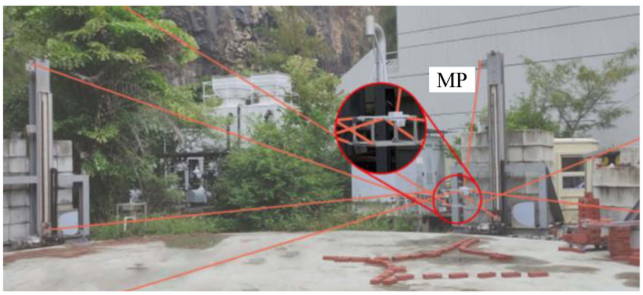

Fig. 23. Photo of the robot on site. The aluminum frame that is hanging in the middle is the MP.

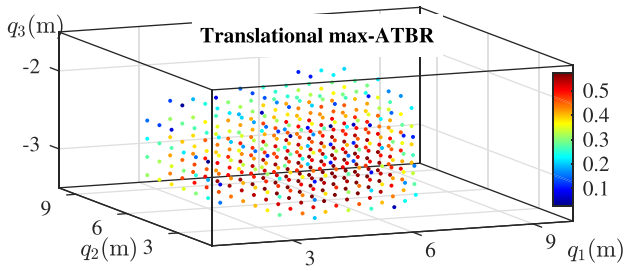

Fig. 24. Distribution max-ATBR showing in translational space, with the MP is always fixed at **0**.

brick-picking and brick-placing. The robot is currently located at The Chinese University of Hong Kong. The overall volume of the robot is around $12 \times 14 \times 4$ m^3. It is designed to build a permanent brick pavilion in a yard. The robot is shown in Fig. 23.

A. Hardware Setup and Motor Curve

The MP is an extruded trapezium with a height of 0.20 m, a short base length of 0.20 m, and a long base length of 0.36 m. It has an extruded thickness of 0.20 m. A gripper is mounted on the MP. During the operation, the total weight of the MP is less than 7 kg.

During robot operation, the motors are constrained by an artificial motor curve, which is adapted from one of the motors on the market (Maxon ECX SPEED 13 M brushless dc Motor). The motor curve is defined by the following four piecewise inequalities:

$$\begin{cases} \overline{f} \le -173.9\dot{l}^2 + 8.6\dot{l} + 94.4 \\ \overline{f} \le -173.9\dot{l}^2 - 8.6\dot{l} + 94.4 \\ |\dot{l}| \le 0.57. \end{cases} \tag{46}$$

The operational region is the intersection of all the equations above. It is shown as the black curve in Fig. 27. To address the possible unexpected motor torque, the modeled motor torque $\overline{f}_m$ is 20% lower than the actually available torque, i.e., $\overline{f}_m \le 0.8\overline{f}$.

B. Max-ATBR Map and Trajectory Generation

This robot focuses on the position of the MP; hence, the orientation is kept constant and the angular velocity is kept at zero all the time. The major required wrench of the robot is the weight from the brick and the MP itself, it is $\boldsymbol{g} =$

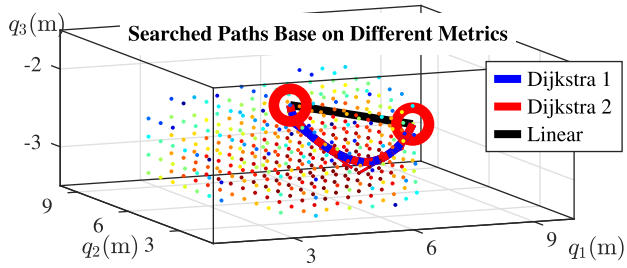

Fig. 25. Searched paths are shown on the max-ATBR workspace. DDAT and max-ATBR return the same path.

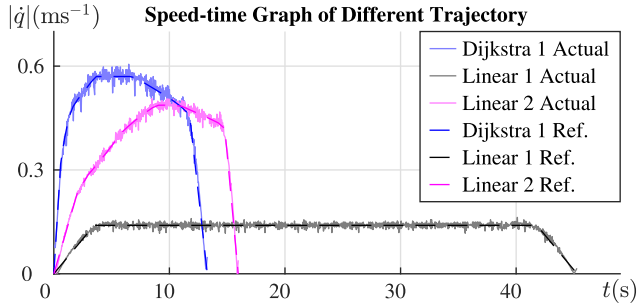

Fig. 26. Speed–time plot for comparing different trajectories. The searching algorithm returns the same path from DDAT and max-ATBR map, named Dijkstra 1. Linear 1 is a linear path with varying speeds. Linear 2 is a traditional path that is generated by a linear trajectory with constant maximum speed. The actual speed–time plot is also shown in the figure as faded solid lines.

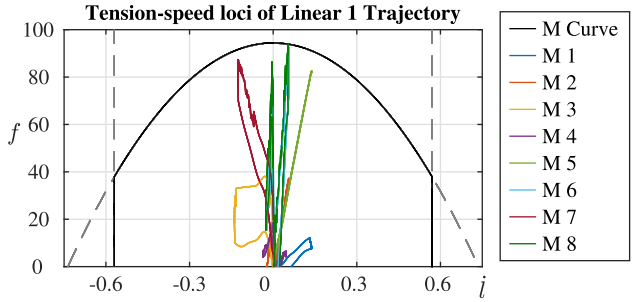

Fig. 27. Loci plot of the cable tension and speed when the MP is running the linear path trajectory with a constant speed. The black line is the motor curve. "M" stands for motor.

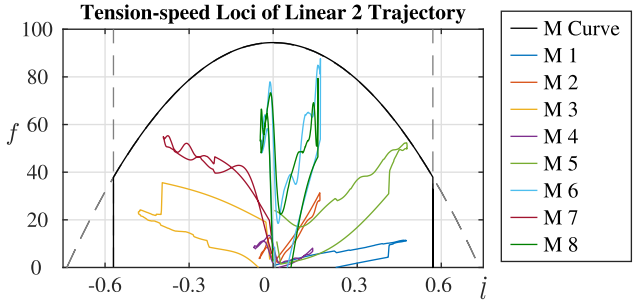

Fig. 28. Loci plot of the cable tension and speed when the MP is running the linear path trajectory with varying speeds. The black line is the motor curve. "M" stands for motor.

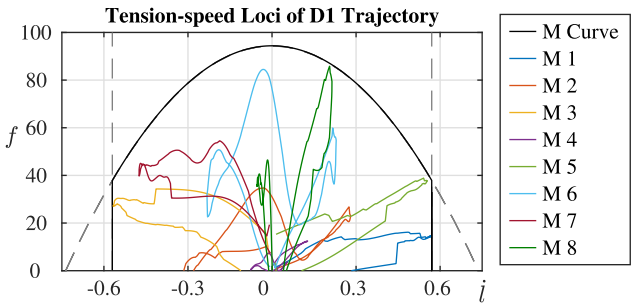

Fig. 29. Another loci plot of the cable tension and speed is shown under the motor curve. The MP is running a trajectory that is searched with the DDAT metric map.

$[0,\ 0,\ 0,\ 68.7,\ 0,\ 0,\ 0]^T$N. To allow the MP to accelerate to adjacent points, two extra RWSs are added to $\boldsymbol{g}$

$$\mathcal{W}_{\mathrm{r}} : \boldsymbol{g} \oplus \boldsymbol{M}(\boldsymbol{q})\overline{\|\ddot{\boldsymbol{q}}\|}\hat{\boldsymbol{q}} \oplus \mathrm{BOX}(10) \tag{47}$$

where $\overline{\|\ddot{\boldsymbol{q}}\|} = 1\,\mathrm{m}\cdot\mathrm{s}^{-2}$ is a conservative magnitude of acceleration. In actual operation, the MP would never perform an acceleration larger than this value. $\hat{\boldsymbol{q}}$ is a set of unit vectors that stores the possible directions to all adjacent points, as defined in (41). The term BOX(10) is a box set with a length of 10 N. The box serves as a safety margin for disturbances and uncertainties.

The rotation is fixed at $[0,\ 0,\ -6.3(10^{-2})]$rad because it is tested that a constant yaw angle generates the largest translational workspace. With a grid of $[15,\ 15,\ 7]$ steps along $q_1, q_2,$ and q_3 axes, respectively, 1575 points in space are evaluated. The translational max-ATBR of this robot is shown in Fig. 24. Although the DDAT is not convenient to be shown in the figure, it is also evaluated.

Two points in the WTFW are selected as the start (brick picking) point and end (brick placing) point. They are $[4.86,\ 5.57,\ -2.23]$ and $[9.42,\ 9.14,\ -2.93]$, respectively. Based on the DDAT and max-ATBR map, the Dijkstra algorithm searches two identical paths as shown in Fig. 25. The generated arc-shaped trajectory is more time-efficient.

From the speed–time graph shown in Fig. 26, the arc-shaped trajectory took 13.3 s, the varying speed linear trajectory took 16.0 s and the traditional constant speed linear trajectory took 45.2 s to complete. The varying speed linear trajectory and arc-shaped trajectory achieve significant 64% and 71% decreases in total traveling time when compared to the traditional method.

The actuation cable tension is also plotted together with the cable speed, which forms a locus plot. The motor curve is also plotted in the same figure for clarity. For the traditional trajectory shown in Fig. 27, some feedback force almost touches the motor curve indicating that these cable force reach their maximum at certain poses. If the torque–speed relationship is ignored, the speed has to be slow to ensure the MP could safely travel through every pose on the path. Therefore, the cable force–speed loci are concentrated in the low-speed area.

The loci of the varying-speed linear trajectory (Linear 2) are more spread out as shown in Fig. 28. It makes use of most of the working region of the motor curve due to the proposed methodology. With the same path, the cable force is similar while the cable speed is allowed to be higher.

Finally, the searched trajectory (D1) improves the traveling time even more by allowing the MP to move through the high-twist region. The loci plot is shown in Fig. 29.

VIII. Conclusion

Considering the torque–speed coupling effect in robot analysis can enhance the capability of the CDPR without any hardware change, largely utilizing the motor capability by considering nonfixed operation points on the motor curve. The MP wrench and twist can be adjusted and compromised with each other based on the MP requirement. This article shows the significance of considering the coupled effect. First, the capability of available twists is increased. Through the new set definition, it is shown that the RWDATS is the superset of the traditional ATS. Second, for any CDPR that has a given wrench and twist requirement, the available workspace volume is larger than the CDPR with traditional calculation, which separates the wrench and twist availability analysis. Third, for a CDPR that has only the wrench requirement, the max-ATBR as a new metric can indicate how fast could the MP travel in operation space. Finally, for fixed task endpoints, the MP traveling time could be decreased by assigning a speed-varying trajectory. The above analysis and applications have been verified on a 6-DoF CDPR hardware, which shows a major improvement in reducing the traveling time of the MP without any hardware changes. Future work will consider the actuator's dynamics in the analysis in order to fully utilize the motors' capabilities. Another improvement is to relax the prerequisite of providing the RWS when calculating the RWDATS, resulting in a new simultaneous wrench–twist available set with higher practicality.

References

[1] J.-P. Merlet, *Parallel Robots*, vol. 128. Berlin, Germany: Springer, 2005.
[2] C. Gosselin, "Cable-driven parallel mechanisms: State of the art and perspectives," *Mech. Eng. Rev.*, vol. 1, no. 12014, Art. no. DSM0004.
[3] C. J. Thompson and P. Campbell, "Tendon suspended platform robot," *Robot. Comput.-Integr. Manuf.*, vol. 13, no. 4, pp. 363–363, 1997.
[4] K. Crolla, P. Cheng, D. Chan, A. Chan, and D. Lau, "Inflatable architecture production with cable-driven robots," in *Proc. Learn., Adapting Prototyping—Proc. 23rd CAADRIA Conf.*, 2018, vol. 1, pp. 9–18.
[5] Y. Wu, H. H. Cheng, A. Fingrut, K. Crolla, Y. Yam, and D. Lau, "Cu-brick cable-driven robot for automated construction of complex brick structures: From simulation to hardware realisation," in *Proc. IEEE Int. Conf. Simul., Model., Program. Auton. Robots*, 2018, pp. 166–173.
[6] L. L. Cone, "Skycam—An aerial robotic camera system," *Byte*, vol. 10, no. 10, pp. 122–132, 1985.
[7] A. Min, "Study on multiple degrees-of-freedom positioning mechanism using wires (Part 1)," *Int. J. Jpn. Soc. Precis. Eng.*, vol. 28, no. 2, pp. 131–138, 1994.
[8] J. Pusey, A. Fattah, S. Agrawal, and E. Messina, "Design and workspace analysis of a 6–6 cable-suspended parallel robot," *Mechanism Mach. Theory*, vol. 39, no. 7, pp. 761–778, 2004.
[9] R. Verhoeven and M. Hiller, "Estimating the controllable workspace of tendon-based Stewart platforms," in *Advance Robot Kinematics*. Berlin, Germany: Springer, 2000, pp. 277–284.
[10] M. Gouttefarde, D. Daney, and J.-P. Merlet, "Interval-analysis-based determination of the wrench-feasible workspace of parallel cable-driven robots," *IEEE Trans. Robot.*, vol. 27, no. 1, pp. 1–13, Feb. 2011.
[11] P. Bosscher, A. T. Riechel, and I. Ebert-Uphoff, "Wrench-feasible workspace generation for cable-driven robots," *IEEE Trans. Robot.*, vol. 22, no. 5, pp. 890–902, Oct. 2006.
[12] E. Stump and V. Kumar, "Workspaces of cable-actuated parallel manipulators," *J. Mech. Des.*, vol. 128, pp. 159–167, 2006.

[13] B. Zi, B. Duan, J. Du, and H. Bao, "Dynamic modeling and active control of a cable-suspended parallel robot," *Mechatronics*, vol. 18, no. 1, pp. 1–12, 2008.
[14] D. Lau, D. Oetomo, and S. K. Halgamuge, "Inverse dynamics of multilink cable-driven manipulators with the consideration of joint interaction forces and moments," *IEEE Trans. Robot.*, vol. 31, no. 2, pp. 479–488, Apr. 2015.
[15] A. Alp and S. Agrawal, "Cable suspended robots: Design, planning and control," in *Proc. IEEE Int. Conf. Robot. Automat.*, 2002, pp. 4275–4280.
[16] J.-P. Merlet and J. A.-d. Sandretto, "The forward kinematics of cable-driven parallel robots with sagging cables," in *Cable-Driven Parallel Robots*. Berlin, Germany: Springer, 2015, pp. 3–15.
[17] S. Lessanibahri, M. Gouttefarde, S. Caro, and P. Cardou, "Twist feasibility analysis of cable-driven parallel robots," in *Cable-Driven Parallel Robots*. Berlin, Germany: Springer, 2018, pp. 128–139.
[18] N. Riehl, M. Gouttefarde, F. Pierrot, and C. Baradat, "On the static workspace of large dimension cable-suspended robots with non negligible cable mass," in *Proc. Int. Des. Eng. Tech. Conf. Comput. Inf. Eng. Conf.*, 2010, pp. 261–270.
[19] M. Gouttefarde and C. M. Gosselin, "Analysis of the wrench-closure workspace of planar parallel cable-driven mechanisms," *IEEE Trans. Robot.*, vol. 22, no. 3, pp. 434–445, Jun. 2006.
[20] G. Abbasnejad, J. Eden, and D. Lau, "Generalized ray-based lattice generation and graph representation of wrench-closure workspace for arbitrary cable-driven robots," *IEEE Trans. Robot.*, vol. 35, no. 1, pp. 147–161, Feb. 2019.
[21] L. Gagliardini, S. Caro, and M. Gouttefarde, "Dimensioning of cable-driven parallel robot actuators, gearboxes and winches according to the twist feasible workspace," in *Proc. IEEE Int. Conf. Automat. Sci. Eng.*, 2015, pp. 99–105.
[22] T. Rasheed, P. Long, D. Marquez-Gamez, and S. Caro, "Kinematic modeling and twist feasibility of mobile cable-driven parallel robots," in *Proc. Int. Symp. Adv. Robot Kinematics*, 2018, pp. 410–418.
[23] H. Jamshidifar, A. Khajepour, and A. H. Korayem, "Wrench feasibility and workspace expansion of planar cable-driven parallel robots by a novel passive counterbalancing mechanism," *IEEE Trans. Robot.*, vol. 37, no. 3, pp. 935–947, Jun. 2021.
[24] H. Jamshidifar and A. Khajepour, "Static workspace optimization of aerial cable towed robots with land-fixed winches," *IEEE Trans. Robot.*, vol. 36, no. 5, pp. 1603–1610, Oct. 2020.
[25] H. Hussein, J. C. Santos, J.-B. Izard, and M. Gouttefarde, "Smallest maximum cable tension determination for cable-driven parallel robots," *IEEE Trans. Robot.*, vol. 37, no. 4, pp. 1186–1205, Aug. 2021.
[26] M. S. Triantafyllou and F. S. Hover, *Maneuvering and Control of Marine Vehicles*. Cambridge, MA, USA: Massachusetts Inst. Technol., 2003.
[27] B. Grünbaum, *Convex Polytopes*, vol. 221. Berlin, Germany: Springer, 2013.
[28] S. Bouchard, C. Gosselin, and B. Moore, "On the ability of a cable-driven robot to generate a prescribed set of wrenches," *J. Mechanisms Robot.*, vol. 2, no. 1, 2009.
[29] M. Gouttefarde and S. Krut, "Characterization of parallel manipulator available wrench set facets," in *Advances in Robot Kinematics: Motion in Man and Machine*. Berlin, Germany: Springer, 2010, pp. 475–482.
[30] I. Ebert-Uphoff and P. A. Voglewede, "On the connections between cable-driven robots, parallel manipulators and grasping," in *Proc. IEEE Int. Conf. Robot. Automat.*, 2004, vol. 5, pp. 4521–4526.
[31] P. Schneider and D. H. Eberly, *Geometric Tools for Computer Graphics*. New York, NY, USA: Elsevier, 2002.

Arthur Ngo Foon Chan (Member, IEEE) received the B.Eng. (Hons.) and Ph.D. degrees in mechanical and automation engineering from The Chinese University of Hong Kong, Hong Kong, in 2017 and 2022, respectively.

He is currently a Postdoctoral Research Fellow with Darwin Lau. His research interests include kinematics and dynamics modeling of cable-driven parallel manipulators, bending structure, and tensegrity robots.

Sabrina Wai Yi Lam received the B.Sc. degree in architectural studies and the M.Sc. degree in mechanical and automation engineering from The Chinese University of Hong Kong, Hong Kong, in 2016 and 2021, respectively.

She is currently a Control Engineer with Roborn, Ltd., Hong Kong. Her research interests include control of cable-driven parallel manipulators, and construction and architectural robotics.

Darwin Lau (Senior Member, IEEE) received the B.Eng. (Hons.) degree in mechatronics engineering, the B.CS. degree, and the Ph.D. degrees in mechanical engineering and robotics from the University of Melbourne, Parkville, VIC, Australia, in 2008 and 2014, respectively.

He was a Postdoctoral Research Fellow with Pierre and Marie Curie University from 2014 to 2015. He is currently an Associate Professor with the Department of Mechanical and Automation Engineering, The Chinese University of Hong Kong, Hong Kong. His research interests include kinematics, dynamics and control of redundantly actuated mechanisms, cable-driven parallel manipulators, construction and architectural robotics, and bioinspired robots.